Chapter 3

EFFECT OF ANGLE-OF-ATTACK ON THE DYNAMICS OF AN INVERTED FLAG

Laboratory and numerical studies have highlighted the potential of exploiting the flapping motion of inverted flags for energy harvesting purposes (Kim et al., 2013; Ryu et al., 2015; Shoele and Mittal, 2016; Silva-Leon et al., 2019). Field realizations of the inverted flag energy harvester, however, have shown that frequent changes in flow direction, characteristic of atmospheric winds, result in reduced harvesting performance (Orrego et al., 2017). Changes in flow direction correspond to variations in the angle of attack of the undeflected flag, which modify its flapping dynamics. This undeflected angle of attack is equal to the angle between the clamping direction of the trailing edge and the direction of the flow and will be referred to as angle of attack for simplicity throughout this text, despite the fact that the instantaneous angle of attack of the flag changes constantly as it deflects. The dynamics of the inverted flag are very susceptible to changes in this angle, as can be deduced from the very different behaviors in the 90- and 180-degree limits. When the flow impinges perpendicularly to the plate, the plate behaves as a bluff body and the main force acting on it is drag, together with any unsteady forces that may arise. These forces can produce large bending deformations that often result in a more streamlined shape, reducing in turn the drag force that the flow exerts on the plate (Vogel, 1994). This phenomenon, named reconfiguration, has been widely studied and is commonly seen in vegetation, preventing breakage and uprooting among other things (De Langre, 2008). Conversely, in the case of a regular flag the flow remains attached and the force that acts perpendicularly to the plate, which is responsible for its bending, is due to lift. The resulting deflection of the plate can subsequently generate flow detachment and unsteady forces. Initially straight, the flag becomes unstable at flow speeds higher than a critical value that is a function of the flag's mass and flexibility (Shelley and Zhang, 2011).

Although these two limit cases have been studied thoroughly, very little information is known about the behavior of cantilever plates at intermediate angles of attack. Preliminary wind tunnel tests have been performed by Cossé et al. (2014) on an inverted flag of aspect ratio 2 at angles of attack of 0, 10 and 20 degrees. At finite α, the flag presented a gradual increase in the amplitude of motion as κ was increased, as

opposed to the zero angle-of-attack case where the flag presents an abrupt increase in amplitude at a single value of κ. The critical κ at which the flag transitioned from the flapping to the deflected regime was found to be different for the three angles. Additionally, the flag at an angle of 20 degrees showed smaller maximum flapping amplitudes than those at smaller angles. This has been corroborated by brief computational studies by Shoele and Mittal (2016) and Tang et al. (2015), who observed the maximum flapping amplitude to decrease abruptly for angles larger than 15 degrees. Interestingly, Tavallaeinejad et al. (2018) studied the related problem of the presence of a small initial zero-stress deflection on the behavior of a small aspect ratio inverted flag clamped at zero degrees. The initial deflection causes the subcritical pitchfork bifurcation to be substituted by a saddle-node bifurcation. This results in the existence of a small deflection steady equilibrium.

While these results highlight some basic changes in the flag's dynamics, the literature lacks a more thorough characterization of the inverted flag's behavior at moderate angles of attack. The purpose of this study is to fully characterize the dynamics of an inverted flag for angles of attack between 0° and 28°, as well as to generate a more comprehensive experimental dataset of the phenomenon. Angles up to 28° have been considered because, as will be shown, the large-amplitude flapping regime disappears beyond that value for a plate of large aspect ratio. The main analysis is performed on a flag of aspect ratio 5 (flag 7, table 1.3). A flag of aspect ratio 2 (flag 8, table 1.3) is subsequently investigated to account for the variability of the results with aspect ratio. Additional measurements on flags of AR=2 and varying mass ratios were performed, but due to limitations in tunnel wind speed and dimensions the variation in μ is quite small. No significant changes were observed in the flag behavior with these small changes in mass ratio and, therefore, no detailed analysis of those flags is presented. Because experimental results on the inverted flag are limited in the literature and the problem has been used in the past as a benchmark for the validation of numerical codes, the obtained data is included in Appendix A as a reference.

3.1 Results

Behavior at zero angle of attack

The results obtained at zero angle of attack are consistent with the existing literature, with the three main dynamical regimes being clearly visible (Kim et al., 2013). Figure 3.1a shows the maximum, minimum and average deflection angle, Φ, for an inverted flag of AR=5 as a function of the square root of the non-dimensional

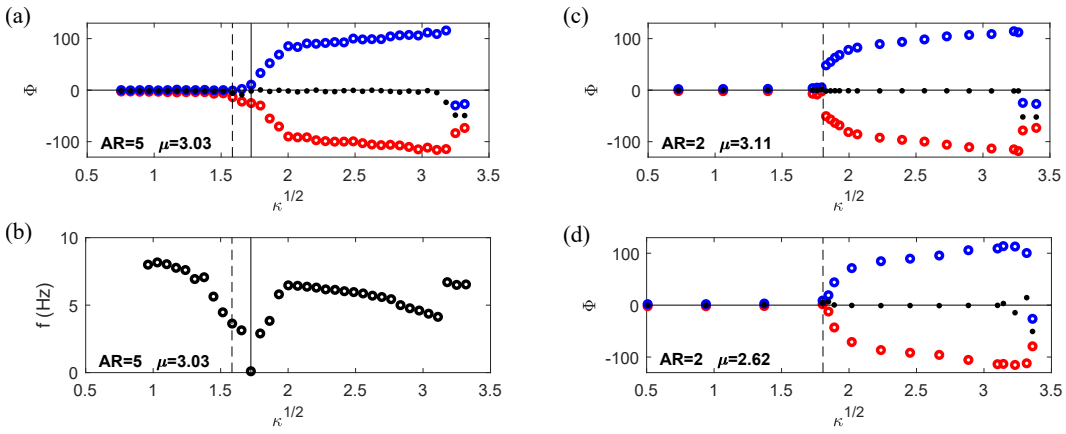

Figure 3.1: Behavior of an inverted flag at zero angle of attack. Maximum (○), minimum (○) and mean (●) deflection angle, Φ, for a flag of (a) AR=5 and $\mu = 3.03$, (c) AR=2 and $\mu = 3.11$ and (d) AR=2 and $\mu = 2.62$. (b) Frequency of motion of the flag of AR=5 and $\mu = 3.03$.

velocity, $\kappa^{1/2}$. At low flow speeds, the flag remains undeflected, undergoing a small amplitude oscillation. As wind speed is increased, it enters the flapping regime, exhibiting a symmetric large-amplitude flapping motion. For the highest values of κ, the flag flexes to the side, oscillating with relatively small amplitude around the deflected position.

As detailed in chapters 1 and 2, the transition from straight to flapping regimes has been proven numerically (Gurugubelli and Jaiman, 2015) and theoretically (Sader et al., 2016a) to be caused by a divergence instability of the zero deflection equilibrium. Figure 3.1b constitutes experimental proof of the existence of this divergence. It displays the frequency of motion of the flag examined in figure 3.1a as a function of non-dimensional wind speed. In the case of the small amplitude oscillations around the zero-deflection equilibrium characteristic of the straight regime, this frequency can be considered to be equal to the flag's natural frequency. In the presence of a divergence instability, the effective stiffness of the flag should asymptote to zero, with the natural frequency thus following the same trend. This is an argument equivalent to that used in Section 2.2. The trend can be clearly observed in figure 3.1b. The value of the oscillation frequency at $\kappa^{1/2} = 1.724$ is equal to $f = 0.1$Hz, indicating the proximity of the divergence point. This experimental value of the divergence velocity has been marked with a solid line in figures 3.1a and 3.1b. The theoretical value obtained using formula (2.10), $\kappa^{1/2} = 1.584$, is in reasonable agreement and is represented for reference with a dashed line.

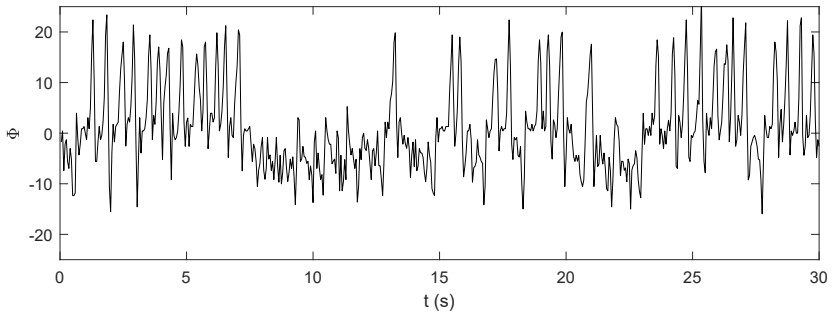

Figure 3.2: Time trace of the deflection angle for an inverted flag of AR=5 in the vicinity of its divergence instability ($\kappa^{1/2} = 1.724$, $f = 0.01$Hz).

As opposed to the results presented in previous experimental studies (Cossé et al., 2014; Huertas-Cerdeira et al., 2018; Kim et al., 2013), the amplitude of motion in figure 3.1a does not increase abruptly after the divergence instability. This discrepancy in post-bifurcation behavior is most likely due to small experimental differences, such as variations in the initial curvature of the flag and states of pre-stress that dampen the flag's motion and reduce its flapping amplitude for the lower velocities. To demonstrate that the discrepancy in post-critical behavior is neither caused by variations in aspect ratio or by variations in mass ratio with respect to the results of Kim et al. (2013), Huertas-Cerdeira et al. (2018) and Cossé et al. (2014), the maximum, minimum and average deflection angles for flags of $\mu = 3.11$ and $\mu = 2.62$ and AR=2 are presented in figures 3.1c and 3.1d, respectively. The experimental divergence velocity, $\kappa^{1/2} = 1.795$, and theoretical divergence velocity, $\kappa^{1/2} = 1.807$, of these flags are almost identical and are represented with a dashed line. Figure 3.1c exhibits a discontinuous jump in amplitude of motion after the divergence, while 3.1d exhibits a gradual increase. Because both flags correspond to the same aspect ratio, the differing behaviors cannot be caused by aspect ratio effects. Additionally, the mass ratio of all three flags is very similar, with the flag of AR=5 (figure 3.1a, $\mu = 3.03$) possessing a mass ratio that is closer to that of the flag presenting an abrupt transition (figure 3.1c, $\mu = 3.11$) than to that of the flag presenting a smooth transition (figure 3.1d, $\mu = 2.62$). It is therefore extremely unlikely that the discrepancy is caused by a mass ratio effect.

It is interesting to note that the amplitude of motion of the flag increases visibly as it approaches the divergence point from the lower velocities (figure 3.1a). This increase does not constitute an increase in oscillation amplitude but rather an increase in perturbation amplitude. As the divergence velocity is approached, the effective

stiffness of the flag becomes lower, and therefore any perturbation will generate larger amplitude deviations. This is demonstrated in figure 3.2, where the time history of the deflection angle at $\kappa^{1/2} = 1.724$, corresponding to the measured velocity closest to the divergence, is plotted. The underlying small-amplitude low-frequency motion is visible. Superimposed are a number of peaks that correspond to the deviations caused by perturbations. They do not possess an inherent frequency and result in broadband noise in the FFT of the signal.

Behavior at finite angle of attack for AR=5

The experimental results obtained for an inverted flag of AR=5 at finite angles of attack are presented in figures 3.3, 3.4, 3.5 and 3.6. Figure 3.3 displays the maximum, minimum and average deflection angle as a function of non-dimensional velocity. Each subfigure corresponds to a different angle of attack, in 2° increments. The value of these angles is specified in the top left corner of each subfigure. Figure 3.4 follows a similar organization and shows the values of the amplitude A', which, as specified in Section 1.2, is calculated as the maximum between $A_{max} - A_{min}$ and $|A_{max}|$ and corresponds to the maximum cross-sectional area of the flag or distance between shed vortices. This parameter offers a reasonable comparison with the amplitude, A, employed in many existing studies, while adding information about the vortex street that is shed. Figure 3.5 shows, in a similar manner, the dimensional dominant frequency of the flag's motion, while figure 3.6 shows the Strouhal number $St = fA'/U$. The frequencies in these last two cases are calculated as the peak of the FFT of the deflection angle's time history. Data is presented only for velocities at which the FFT presented a clear peak. In certain cases, two distinct peaks are present; the largest peak was taken as the dominant frequency. Because the amplitude of these peaks is similar, small changes result in the switching of the dominant peak. This is reflected as a jump in the represented frequency. An example are the last four points of figure 3.5 at $\alpha = 6°$, whose FFTs are represented in the last four plots of figure 3.7.

The characteristics of the AR=5 flag's dynamics at these moderate angles of attack will be analyzed in the following sections. The case of the flag at an angle of attack $\alpha = 6°$ will be used as an example throughout, with similar general characteristics being present for all angles. The evolution of the flag's behavior with angle of attack will then be discussed in Section 3.1.

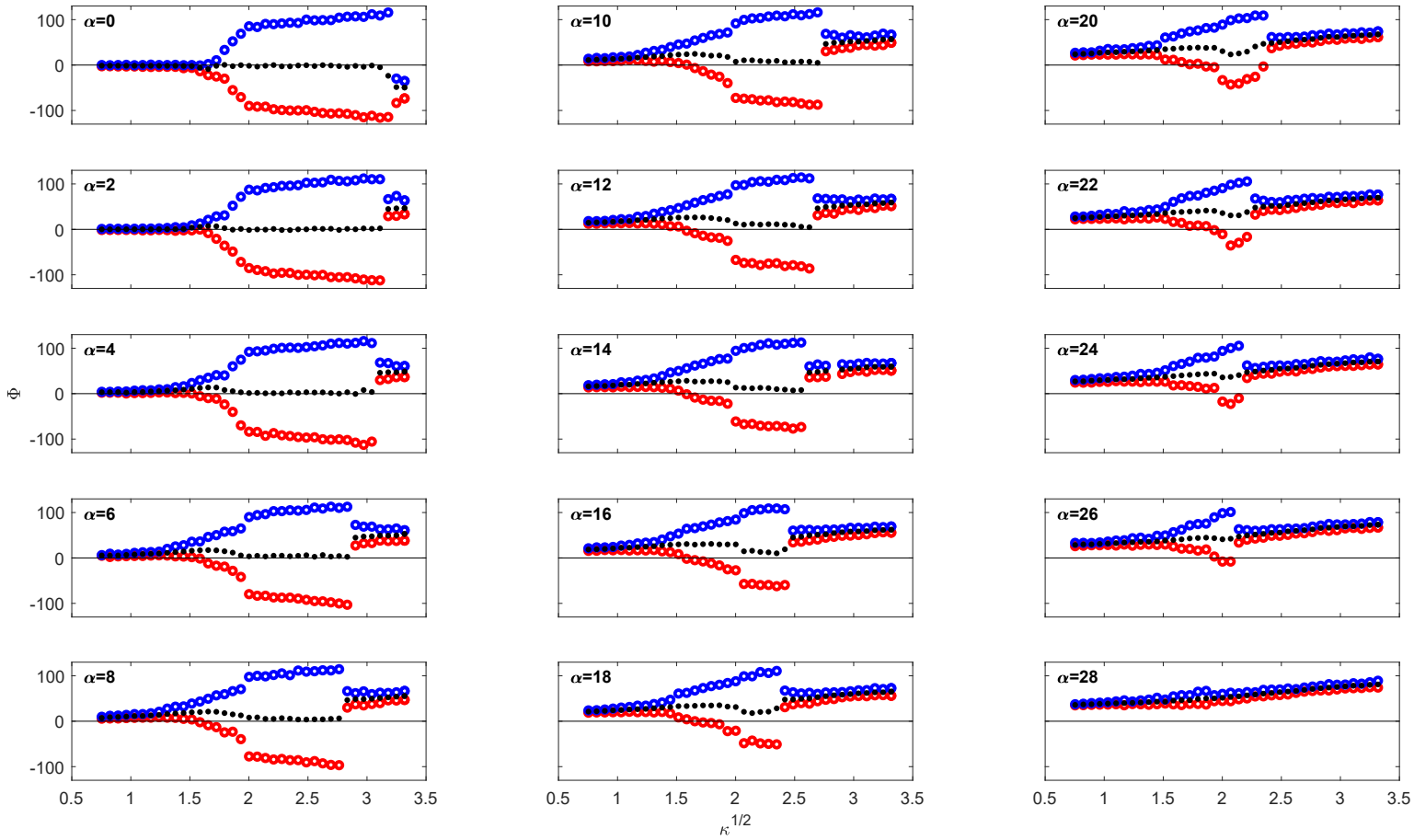

Figure 3.3: Maximum (○), minimum (○) and mean (●) deflection angle, Φ, for an inverted flag of AR=5 and $\mu = 3.03$ as a function of non-dimensional flow velocity, κ, and angle of attack, α

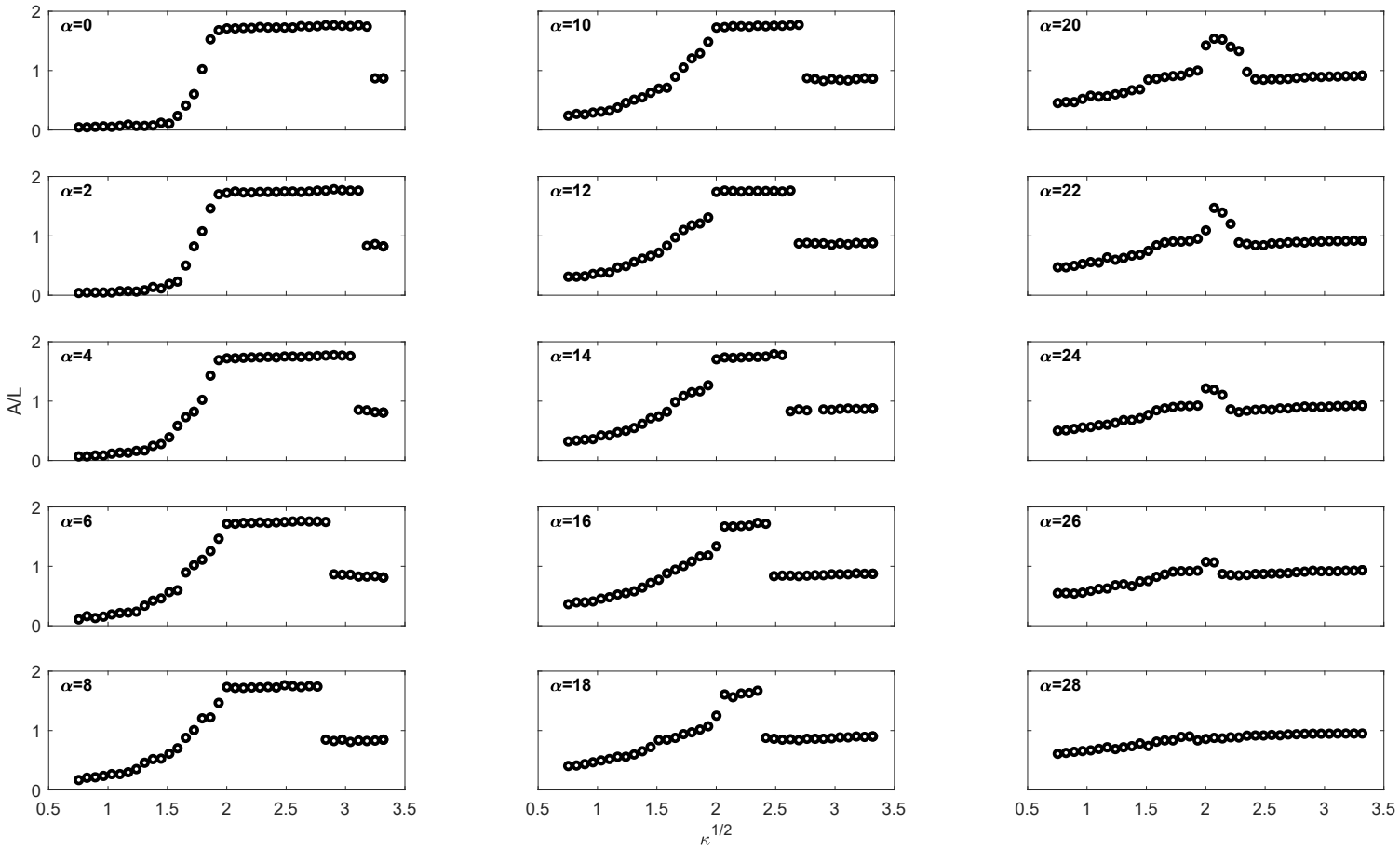

Figure 3.4: Maximum cross section, A', for an inverted flag of AR=5 and $\mu = 3.03$ as a function of non-dimensional flow velocity, κ, and angle of attack, α

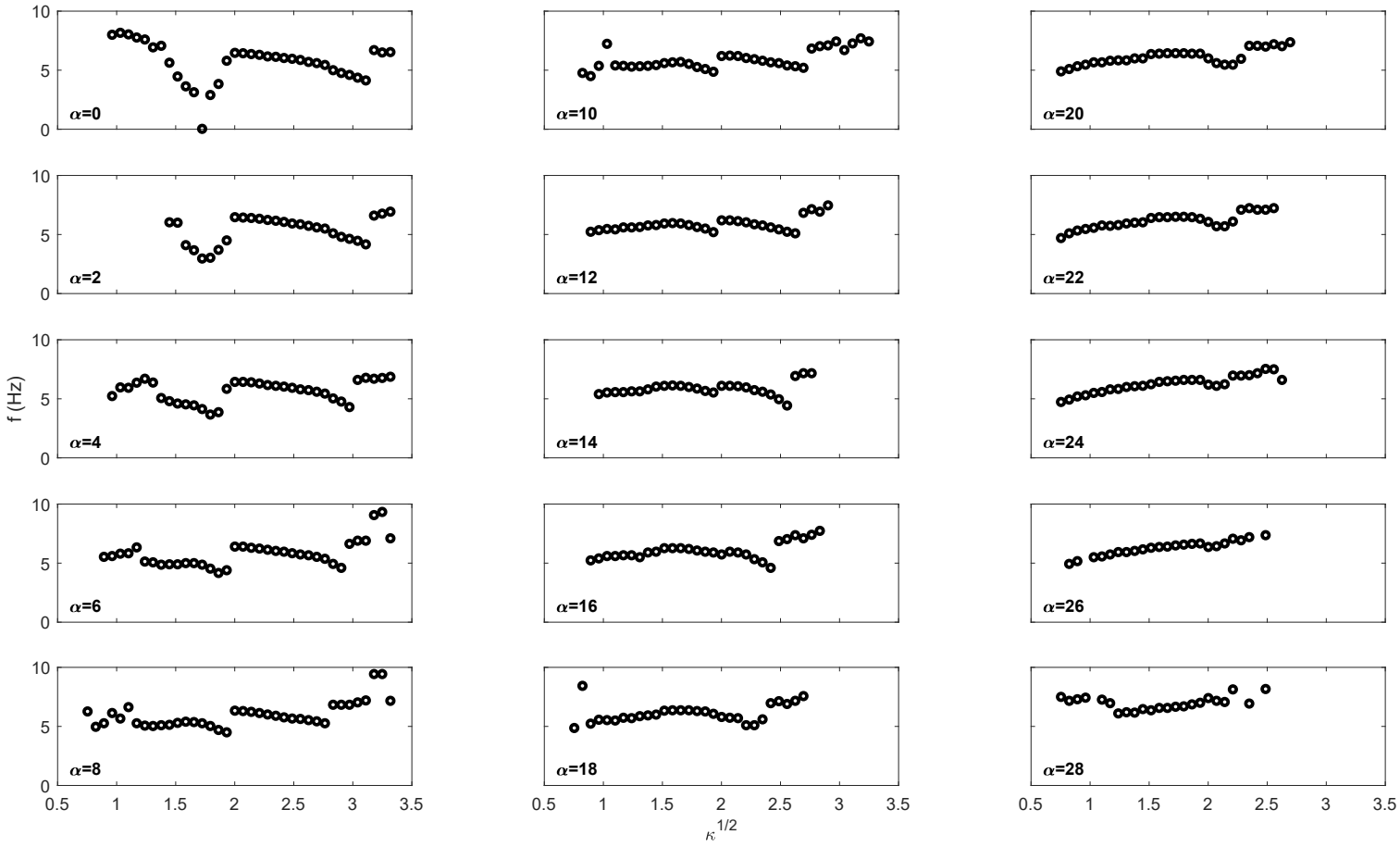

Figure 3.5: Frequency of motion, f, for an inverted flag of AR=5 and $\mu = 3.03$ as a function of non-dimensional flow velocity, κ, and angle of attack, α

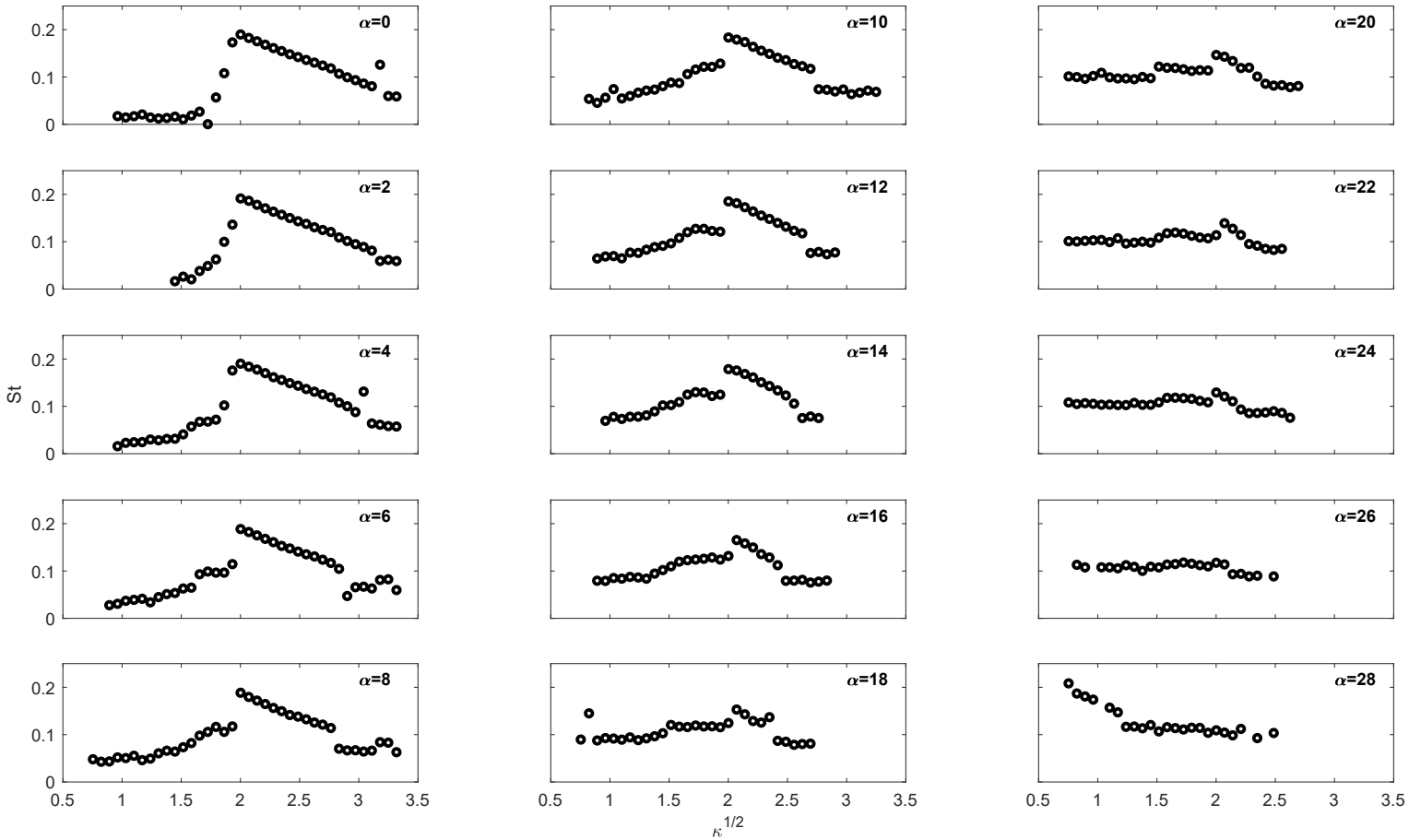

Figure 3.6: Strouhal number, $St = fA'/U$, for an inverted flag of AR=5 and $\mu = 3.03$ as a function of non-dimensional flow velocity, κ, and angle of attack, α

Deformed regime

As is expected, inverted flags clamped at finite angles of attack do not present a straight regime. For small values of κ, these flags undergo a small-amplitude oscillation around a small-deformation deflected equilibrium (figure 3.3). This regime will be denominated deformed in this text to make a distinction from the larger-deformation deflected regime. It is similar to the biased regime, that has been reported under several denominations in computational studies at zero angle of attack (Goza et al., 2018; Gurugubelli and Jaiman, 2015; Ryu et al., 2015) but is absent in the experimental literature. The lack of experimental observations may be due, however, to the difficulty of experimentally distinguishing between strictly zero and very small deflections as well as to the presence of small initial plate curvatures. The fundamental difference between deformed and straight regimes lies in the response to flow velocity of the equilibrium position around which the flag oscillates. In the case of the deformed regime, the deflection of this equilibrium increases with κ, remaining constant at $\Phi = 0°$ for all κ in the case of the straight regime. While inverted flags clamped at $\alpha = 0°$ transition from straight to deformed modes at a finite flow velocity (Gurugubelli and Jaiman, 2015; Ryu et al., 2015), flags at an angle of attack are inherently deformed for all flow speeds.

Although the dynamics of the inverted flag in the deformed regime are similar for all angles of attack, i.e., small oscillations around the deflected position (figure 3.3), the flow behavior exhibits significant changes. For small angles of attack ($\alpha \lesssim 10$) and low wind speeds, the deflection of the flag is small, and the flow remains attached. As wind speed is increased the deflection increases accordingly, reaching a critical value at which the flow separates. For the larger angles of attack ($\alpha \gtrsim 12$), the flow is separated for all wind speeds within the studied range. Flow separation results in modified lift and drag forces on the flag, modifying the equilibrium position around which the flag oscillates. The unsteadiness of the deflected flow, however, does not present a frequency similar to the natural frequency of the flag, and no large flapping is induced. The flow velocity, κ, at which the flow separates can be identified in figure 3.5. The small oscillations present in the deformed regime are caused by the flow unsteadiness from both turbulence and vortex shedding and occur at the effective natural frequency of the flag. This natural frequency is dependent on the damping produced by the flow. Because the aerodynamic forces are modified when flow separation occurs, the effective natural frequency, and consequently oscillation frequency, should present an abrupt change at the separation velocities. This jump

can, effectively, be observed in figure 3.5 for $\alpha = 2° - 10°$ at low values of κ. The maximum deflection angle of the flag's oscillation for the flow speeds at which this jump occurs, κ_{sep}, is $\Phi = 8.8°,\ 9.8°,\ 13.0°,\ 12.4°$ and $15.1°$ at the angles of attack $\alpha = 2°,\ 4°,\ 6°,\ 8°$ and $10°$, respectively. These deflection angles are within the range expected for separation to occur. Variations in the separation deflection angle for different angles of attack may be caused by several factors, including the varying flow velocity and corresponding turbulence intensity at separation, the varying flag geometry resulting from the differing angle of attack and deformation mode shape, and experimental errors in both deflection angle and non-dimensional flow velocity.

The presence of a divergence instability, associated to the cessation of the straight regime, is no longer observed at finite angle of attack. As can be corroborated in figure 3.5, no decay to $f = 0$ of the oscillation frequency occurs. Instead, as κ is increased the amplitude of the flag oscillations begins to grow, and a large amplitude flapping motion develops. The nature of this flapping motion is analyzed in Section 3.1.

Flapping regime

The lack of a divergence instability and the gradual increase of the flag's oscillation amplitude pose a challenge in defining a critical transition velocity, κ_{lower}, from deformed to flapping regimes. The method proposed by Cossé et al. (2014) defines κ_{lower} as the speed at which the flag reaches an amplitude of motion that is a specified fraction of the maximum flapping amplitude. The selection of this fraction, however, is arbitrary, and variations in fraction result in significant changes in the value of the critical velocity. An alternate approach, based on the FFT of the flag's deflection angle, is suggested here. As an example, the FFTs of the motion of a flag at $\alpha = 6°$ and varying κ are shown in figure 3.7. The difference between flapping motions, where the FFT shows a crisp peak, and motions with no resonance, where the FFT appears noisy even if a peak is present, is distinguishable by eye. The flapping regime is therefore defined as the range of wind speeds at which these FFTs present a crisp peak. In order to mathematically define this region, a bi-Gaussian function is fitted to each FFT, normalized such that its maximum value is equal to one, and the sum of squares error (SSE) is calculated

$$SSE = \sum_{1}^{n} (y_i - \psi(f_i))^2 \tag{3.1}$$

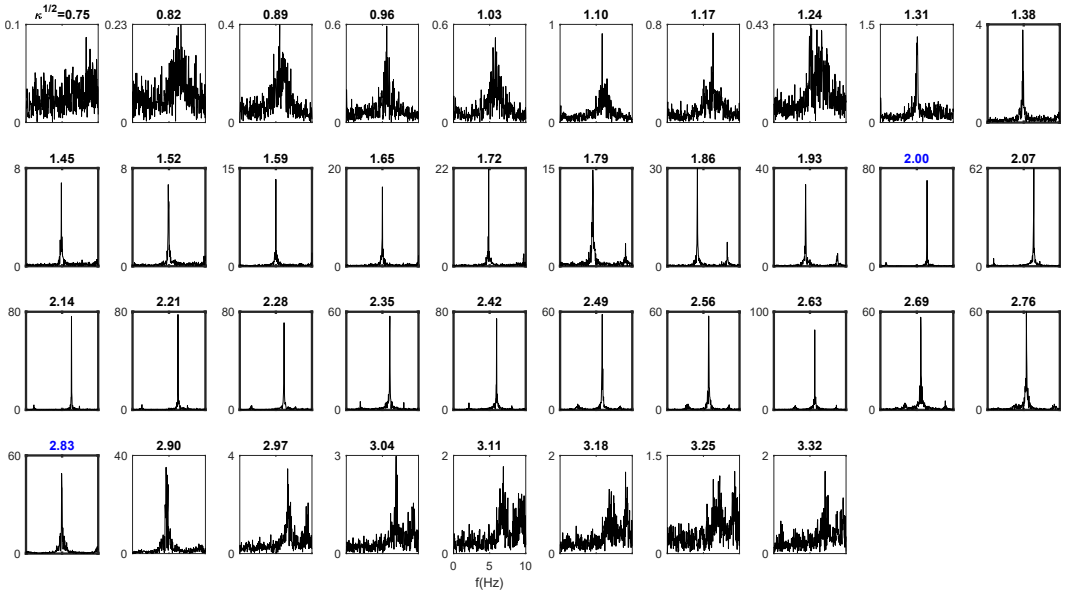

Figure 3.7: Power spectra of the inverted flag's motion for $\alpha = 6°$ and varying flow velocities. The velocities highlighted in blue correspond to the beginning and end of the upper branch large amplitude flapping motion. The velocities highlighted with a bold frame correspond to the flapping regime as defined by equation (3.2).

where n is the number of points in the FFT, y_i is the value of the FFT at the frequency f_i and $\psi(f_i)$ is the value of the fit at f_i. The SSE provides a measure of the dispersion of the function around the fit, which in this case is correlated to the dispersion or "noisiness" of the FFT. The value of the SSE obtained for the fits in the $\alpha = 6°$ case is plotted in figure 3.8a. The SSE displays a low-value plateau at the flapping velocities, with its value increasing in the deformed and deflected regimes. Consequently, the flapping regime has been defined as the range of κ at which

$$SSE\left(\frac{FFT}{max(FFT)}\right) < 1 \tag{3.2}$$

The FFTs corresponding to the flapping regime, as defined by equation (3.2), have been identified with a bold frame in figure 3.7. The limits of this flapping region are marked with black vertical lines in figure 3.8b, that illustrates the maximum, minimum and average deflection angle for the motion of the $\alpha = 6°$ flag. While the transition from deformed to flapping regimes is smooth, the transition from flapping to deflected regimes is well defined and corresponds to an abrupt decrease in the amplitude of motion. The limits defined by equation (3.2) capture this transition and the overall flapping region reasonably well. A single data point is present in figure

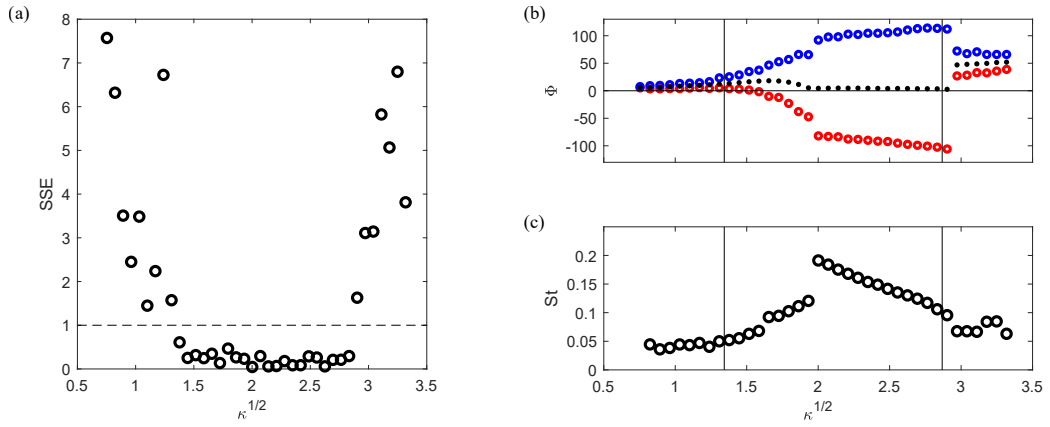

Figure 3.8: Definition of the flapping region for an inverted flag at $\alpha = 6°$ (a) SSE for a bi-Gaussian fit to the power spectra of the flag's motion (○) and threshold defining the flapping regime (-) (b) maximum (○), minimum (○) and mean (●) deflection angle, Φ, with limiting flow velocities for the flapping region (black lines) and (c) Strouhal number with limiting flow velocities for the flapping region (black line)

3.8b that shows a large-amplitude motion and is located beyond the limit established for the flapping range. This point corresponds to a bi-stable region, where both flapping and deflected motions are possible. This region will be studied in more detail in Section 3.1. The disparity in figure 3.8b is not coincidental; it stems from utilizing different data sets for the calculation of the SSE and the deflection angle and highlights the slight mobility of the defined upper critical velocity κ_{upper}. It is important to note that the threshold specified in equation (3.2) is relevant for the data employed in this chapter, but may need to be adjusted for different data sets depending on the noise level, frame rate employed and total number of frames acquired. It is, however, not arbitrary, unlike the maximum-amplitude fraction employed by Cossé et al. (2014), and is chosen such as to separate the existing plateau. Alternative approaches to identifying this flapping region are certainly possible, and a more rigorous approach may be developed as our knowledge of the underlying physics expands. The outlined procedure produces, however, reasonable results with the available data and large discrepancies should not be expected when utilizing alternative criteria.

The existence of two distinct regions within the flapping regime is easily recognizable from figure 3.8b and figure 3.8c, which displays the Strouhal number of the flag's motion for the same $\alpha = 6°$ flag. The first region will be denominated lower branch and is present between $\kappa_{lower}^{1/2} < \kappa^{1/2} < 2$ in figures 3.8b and 3.8c. The second

region, which will be denominated upper branch, lies between $2 < \kappa^{1/2} < \kappa^{1/2}_{upper}$. The two regions are separated by an abrupt shift in amplitude and Strouhal number.

The upper branch corresponds to the large-amplitude flapping motion present at zero angle of attack and thoroughly described in the inverted-flag literature. It possesses all of the traits characteristic of a vortex-induced vibration, as established by Sader et al. (2016a). The peak Strouhal number occurs at $\kappa^{1/2} = 2$ and is between St=0.19–0.18 for angles up to $\alpha \approx 15°$, decreasing rapidly for larger angles of attack (figure 3.6). These values are characteristic of lock-on in VIVs, marking the synchronization of vortex shedding, oscillation frequency and natural frequency. In this upper branch the angular deflection, $\Delta\Phi$, increases with flow speed, but the amplitude A' is roughly constant as a result of the problem's geometry (figure 3.4), with increased deflections resulting in the flag bending backwards. The frequency decreases slightly as flow speed is increased, as is characteristic of vortex-induced vibrations in heavy fluid loading. As a result the Strouhal number decreases practically linearly as wind speed is increased, until the shedding frequency reaches values disparate enough from the flag's natural frequency that the lock-on is lost (Goza et al., 2018).

The lower branch, on the other hand, exhibits notably different features. The Strouhal numbers within this branch vary between St=0.02 and St=0.13. They show a significant increase as flow speed is raised as a result of the comparably rapid increase in amplitude. Neither of these characteristics are indicative of a vortex-induced vibration. A different resonant phenomenon must therefore be the underlying cause of the large-amplitude flapping motion. The FFTs of the flag's motion for velocities in the deformed regime, leading to the appearance of the lower branch, are visible in figure 3.7 for the $\alpha = 6°$ case. They present a single peak that increases in amplitude as the critical velocity κ_{lower} is approached. For the highest angles of attack ($\alpha > 20$), two peaks are present (not pictured here), however, they do not approach each other, with a single peak increasing in amplitude as the lower branch is neared. The lack of a second coalescing peak makes the presence of a coupled-mode flutter instability unlikely. Additionally, it is interesting to note the behavior of the minimum deflection angle throughout the velocity range corresponding to this branch (figures 3.8b and 3.3). At the lower velocities, the minimum deflection is positive, albeit small, and the flag does not surpass the zero deflection position. For the larger velocities, on the other hand, the minimum deflection reaches relatively large negative values. As an example, the highest and lowest minimum deflections at $\alpha = 6°$ are $\Phi = 3°$ and $\Phi = -50°$, respectively. It therefore seems reasonable

to assume that the shedding of vorticity and resulting wake are qualitatively very different for different velocities within the lower-branch range. This would eliminate the synchronization between the flag's natural frequency and the frequency of the unsteady fluid forcing as a probable driving mechanism. These observations point in the direction of a single-mode galloping instability. Figure 3.9a shows the lower critical velocity at which the lower branch develops (green triangle) together with the separation velocity (black triangle) for all angles of attack. It demonstrates that at the emergence of the lower branch the inverted flag always sees separated flow and thus the quasi-steady forcing on the flag is non-linear. It is therefore possible that the lower branch is the result of a stall-flutter mechanism. Further investigations, however, are necessary to unequivocally characterize the nature of this instability. It should be highlighted that the flags at high angles of attack ($\alpha > 16$) present a discontinuity in flapping amplitude and frequency at a constant value of $\kappa^{1/2} \approx 1.5$, which may indicative of a transition to a different driving mechanism within the lower branch.

Deflected regime

The fluid damping on an inverted flag that is flapping within the upper branch grows with increasing flow speed, reducing the flag's effective natural frequency. When the value of this natural frequency is disparate enough from the vortex shedding frequency, the flag's motion ceases to lock-on to the vortex shedding frequency and the large-amplitude flapping motion disappears, giving rise to the deflected regime. This lock-off occurs at $St \simeq 0.08$ for the smallest angles of attack ($\alpha \leqslant 4$) and at $St \simeq 0.11$ for the larger angles (figure 3.6). Between flapping and deflected regimes, a bi-stable region, where either regime is possible, was observed. In certain cases, the position of the flag was either flapping or deflected depending on initial conditions, while in other cases the flag switched randomly from one mode to the other, resulting in the chaotic regime that has been reported for inverted flags at zero angle of attack (Goza et al., 2018; Sader et al., 2016a). This bi-stable region was only observed to exist at small angles of attack $\alpha \lesssim 8^\circ$ and occurred for a narrow band of flow velocities.

The critical velocity, κ_{upper}, at which the flag enters the deflected regime, decreases with angle of attack (figure 3.3). An interesting observation was made by Cossé (2014): independently of angle of attack, the inverted flag shows a similar shape at the emergence of the deflected regime. This is quantitatively corroborated in

α (°)	$\bar{\Phi}_{def}$ (°)
0	48.5
2	44.8
4	46.0
6	44.8
8	46.6

α (°)	$\bar{\Phi}_{def}$ (°)
10	46.6
12	46.2
14	46.8
16	45.3
18	47.7

α (°)	$\bar{\Phi}_{def}$ (°)
20	48.5
22	47.9
24	47.3
26	47.1
Mean	46.7 ± 1.2

Table 3.1: Mean deformation angle of the inverted flag at the emergence of the deflected regime

the present measurements. Table 3.1 shows the average deflection angle, $\bar{\Phi}$ at the wind speed at which the flag first enters the deflected regime. The value of this average deflection is virtually constant, with an average of $\bar{\Phi} = 46.7°$ and a standard deviation of $\sigma = 1.2°$. No trend is visible within these small variations.

The velocity, κ_{def} at which the flapping regime ends is plotted in figure 3.9a together with the velocity at which the synchronized motion ceases, κ_{upper}, as defined by equation (3.2). In this case both velocities correspond to the same dataset, eliminating any disparities due to the bi-stable nature of the flag in this region. For most angles of attack, both velocities coincide; within the region $\alpha = 15° - 20°$ synchronization is lost before the flag enters the deflected regime. This is reminiscent of the result obtained by Goza et al. (2018), who reported large-amplitude flapping without classical VIV for the highest velocities within the flapping range for the zero angle-of-attack case. Interestingly, the FFT of the flag's motion (figure 3.7) transitions from presenting a single dominant peak in the deformed and flapping regimes to presenting two clear peaks in the deflected regime. The frequency of the second peak, however, is too low to correspond to the vortex shedding frequency, but may correspond to subharmonics of the unsteady fluid forces.

Evolution with angle of attack

The three main dynamical regimes present in the motion of inverted flags at moderate angles of attack (deformed, flapping and deflected) have been analyzed in detail in the previous sections. Figure 3.9a displays the range of flow velocities at which each regime occurs for the different angles of attack, with κ_{lower} (green triangle) marking the transition from deformed to flapping regime and κ_{def} (black rhombus) marking the transition from flapping to deflected regime.

For angles of attack up to $\alpha = 14°$ the lower critical velocity decreases practically linearly as α is increased. Between $14° < \alpha < 22°$ this velocity remains mostly

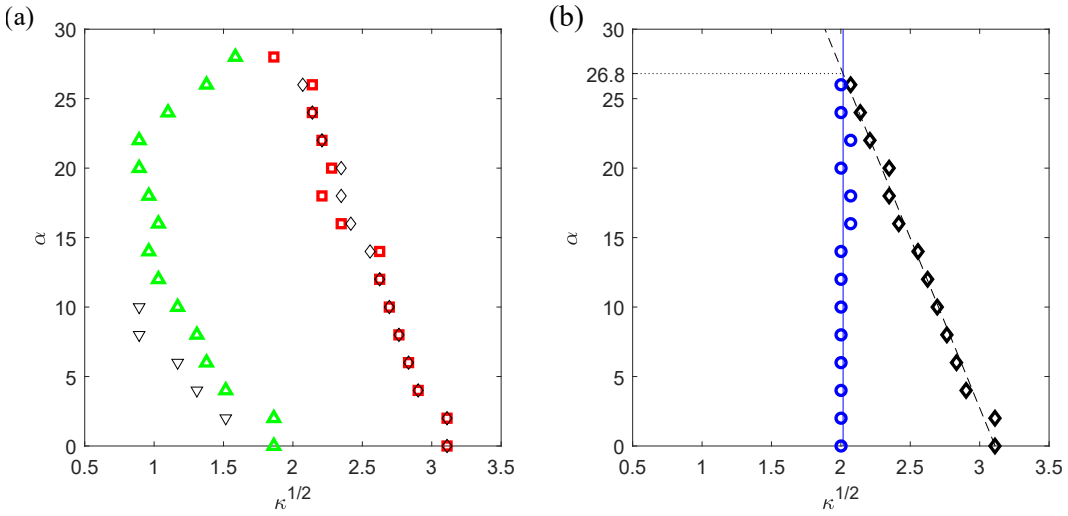

Figure 3.9: Critical non-dimensional flow velocities as a function of angle of attack (a) Separation velocity, κ_{sep} (∇), beginning of resonance, as defined by equation (3.2), and flapping regime, κ_{upper} ($\triangle$), end of resonance, κ_{lower} ($\square$), and deflection velocity, κ_{def} ($\diamond$). (b) Beginning of upper branch (VIV) flapping ($\circ$) and deflection velocity ($\diamond$) with linear fits.

constant to subsequently rapidly increase for angles $\alpha > 22°$. This variation in trend may be caused by changes in the underlying mechanisms behind the flapping motion for varying angles of attack. Further understanding of these underlying mechanisms, however, is required to clarify this behavior. The deflection velocity, κ_{def}, decreases with angle of attack, most likely due to the increased flow damping exerted when flags are at larger angles to the flow. This decrease is surprisingly linear with angle of attack. Even more surprisingly, the velocity at which the flag enters the upper branch of the flapping regime (VIV) is constant for all α, at a value of $\kappa^{1/2} = 2$.

The flow velocities at which the upper-branch vortex induced vibration is initiated and terminated are plotted in figure 3.9b, together with linear fits to the data. Because the starting velocity is constant and the ending velocity decreases with angle, at a specific angle of attack both velocities become equal and the upper-branch disappears. The value of this angle, calculated utilizing the linear fits, is $\alpha = 26.8°$ for the flag studied. Effectively, at angles larger than this value, such as $\alpha = 28°$ represented in figures 3.3, 3.4, 3.5 and 3.6, this motion is no longer present. The lower-branch flapping motion is present at angles beyond this value, but not significantly higher. For $\alpha \approx 28°$ the lower and upper critical velocities meet, and the flapping regime ceases to exist overall (figure 3.9a). At these angles the deformed and deflected regimes merge into a single common regime, where the

flag flexes with continuously increasing deflection angle and oscillates with small amplitude around this position.

At any given free-stream velocity within the upper branch, the angular amplitude of motion of the flag remains approximately constant with angle of attack for angles $\alpha \leqslant 14°$, with the amplitude decreasing rapidly for angles beyond that value (figure 3.3). This result is in agreement with the threshold obtained by Shoele and Mittal (2016), who observed the amplitude of motion to notably decline for angles beyond $\alpha = 15°$. Because the maximum angular amplitude occurs at the highest flow velocity before deflection and the value of this velocity decreases with angle of attack, the overall maximum angular amplitude decreases with angle of attack for all angles. The Strouhal number follows a similar trend, diminishing rapidly for angles beyond $\alpha = 14°$ (figure 3.6). The energy harvesting performance of the inverted flag is therefore severely limited beyond this value, both due to the decrease in the flapping amplitude and the decrease in range of velocities at which flapping occurs.

Behavior at finite angle of attack for AR=2

The experimental measurements performed in Section 3.1 for an inverted flag of aspect ratio AR=5 were reproduced for a flag of AR=2. The results are presented here, with the objective of highlighting the most prominent differences. The obtained data is presented in a similar manner: the maximum, minimum and mean deflection angle, Φ, is shown in figure 3.10, the cross section amplitude, A' , in figure 3.11, the frequency, f, in figure 3.12 and the Strouhal number, St, in figure 3.12. The corresponding values for the AR=5 flag are included for comparison in these figures.

The three main dynamical regimes present in the motion of the flag of AR=5 (deformed, flapping and deflected) can be recognized in the motion of the AR=2 flag. At low flow velocities, the flag oscillates around a small deflection equilibrium. In this case, the power spectra of the motion present two clear peaks, that may be indicative of the effect of the second length scale (height, H). These two frequencies are visible, for example, at the lower velocities of the $\alpha = 2°$ case in figure 3.12, where the jump between two frequency levels corresponds to the switching of the dominant peak. The flow detachment velocity is no longer visible at small angles of attack, which suggests lower detachment velocities that are not within the evaluated range. The transition to the flapping regime occurs in a similar manner to the higher aspect ratio case, with the lower of the two frequency peaks growing in amplitude and no coalescence of peaks being observed.

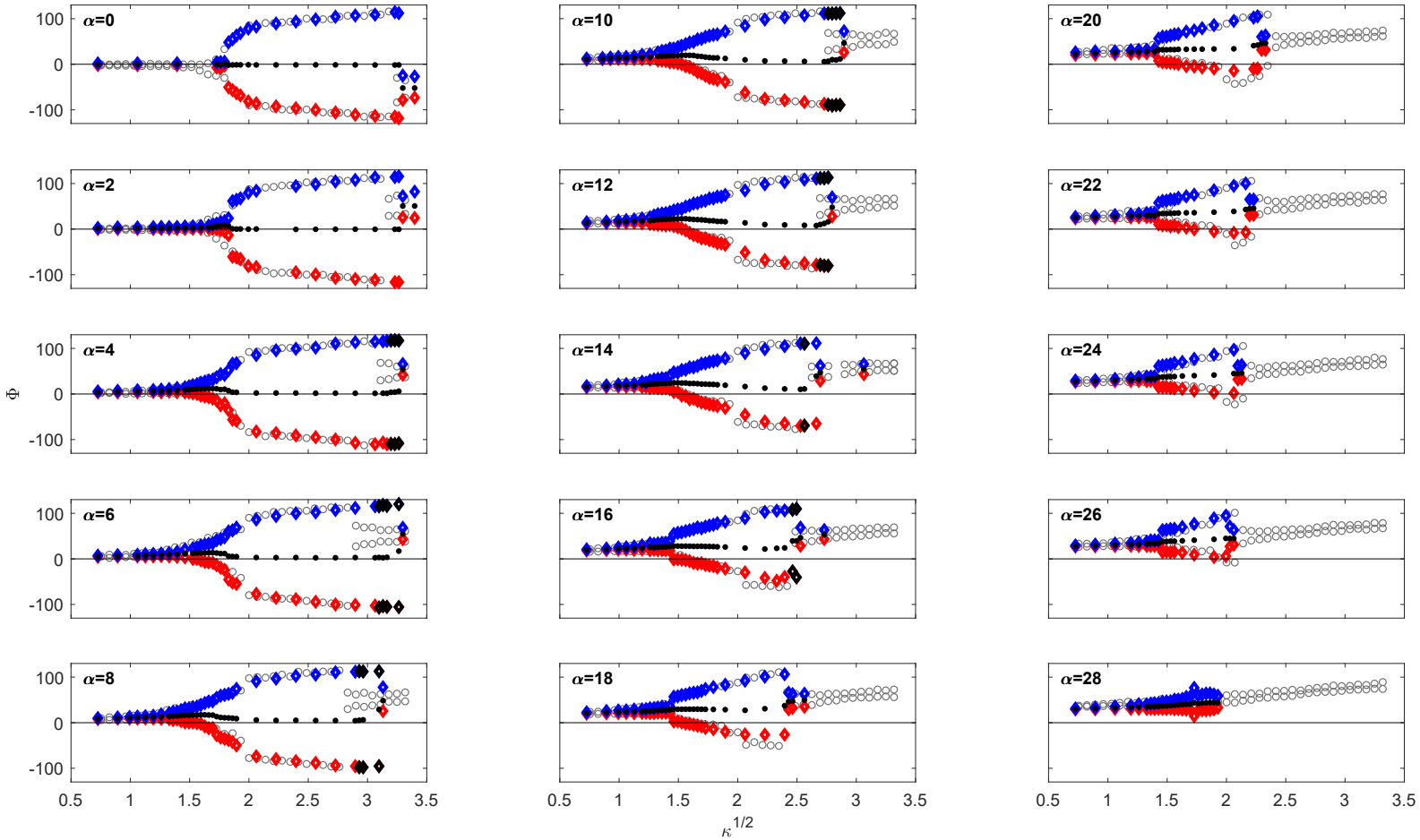

Figure 3.10: Maximum (◇), minimum (◇) and mean (•) deflection angle, Φ, for an inverted flag of AR=2 and $\mu = 3.11$ as a function of non-dimensional flow velocity, κ, and angle of attack, α. Maximum and minimum deflection angle for an inverted flag of AR=5 (○).

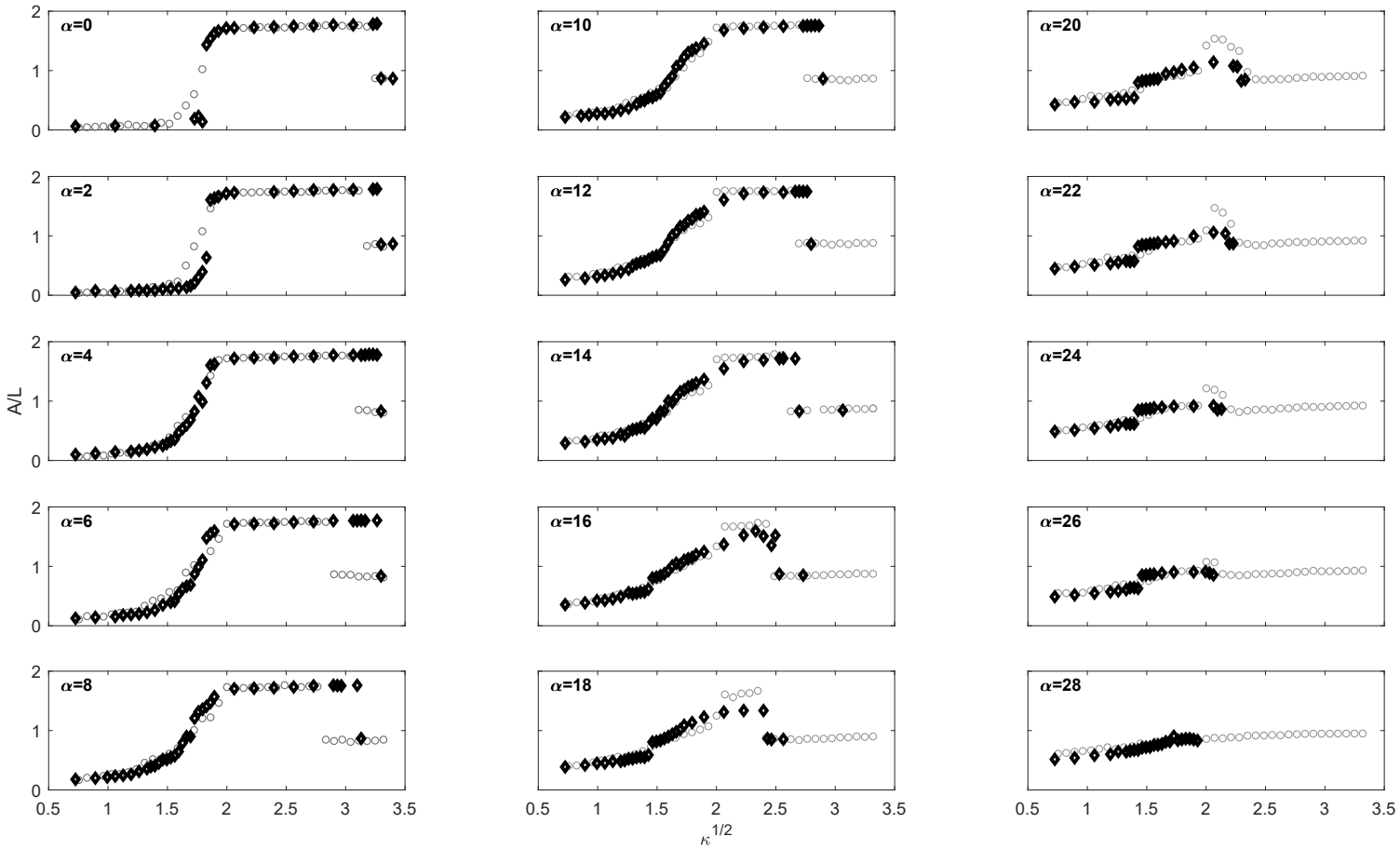

Figure 3.11: Maximum cross section, A'($\diamond$), for an inverted flag of AR=2 and μ = 3.11 as a function of non-dimensional flow velocity, κ, and angle of attack, α. Maximum cross section for an inverted flag of AR=5 ($\circ$) for reference.

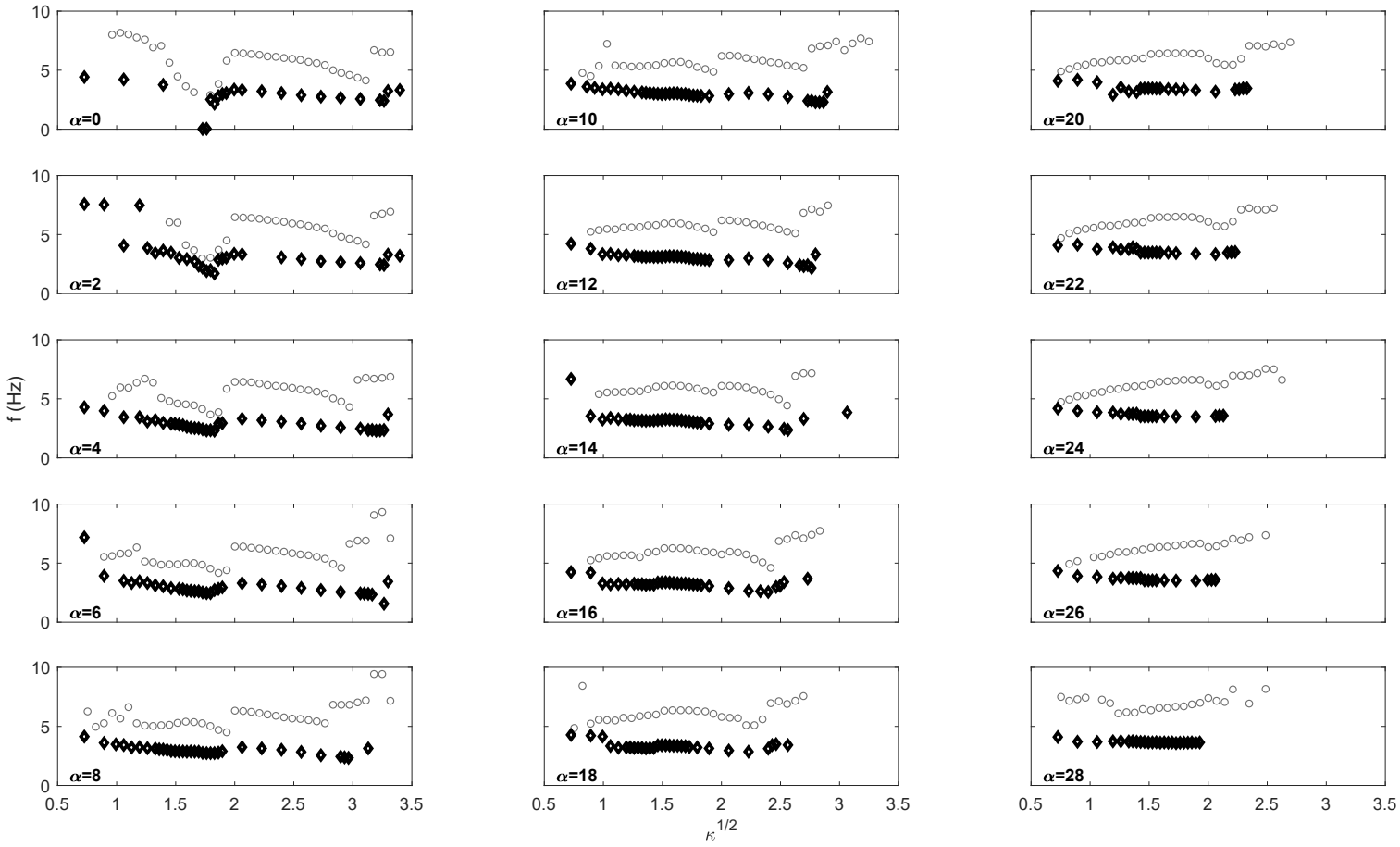

Figure 3.12: Frequency of motion, f ($\diamond$), for an inverted flag of AR=2 and $\mu = 3.11$ as a function of non-dimensional flow velocity, κ, and angle of attack, α. Frequency of motion for an inverted flag of AR=5 ($\circ$) for reference

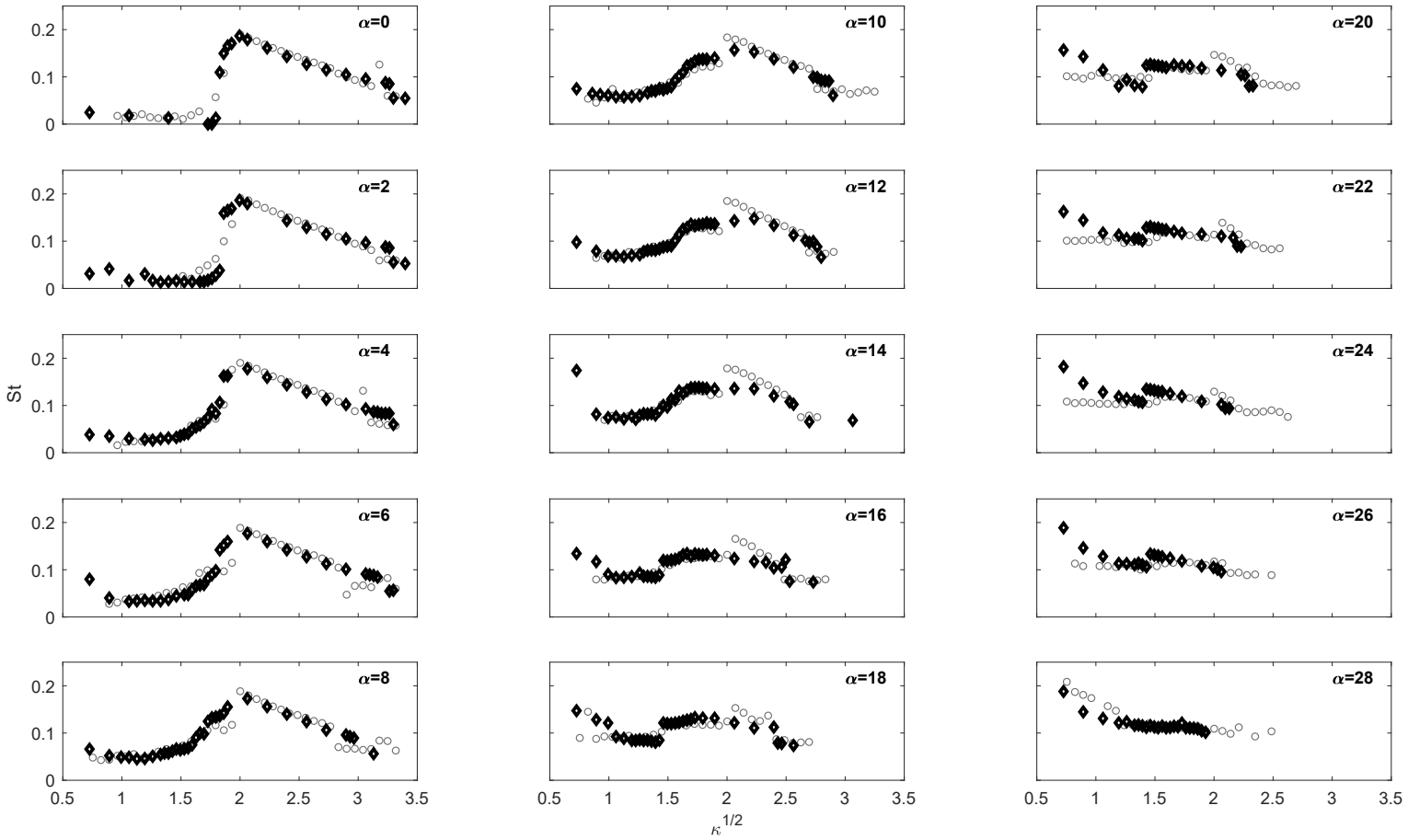

Figure 3.13: Strouhal number, $St = fA'/U$ ($\diamond$), for an inverted flag of AR=2 and $\mu = 3.11$ as a function of non-dimensional flow velocity, κ, and angle of attack, α. Strouhal number for an inverted flag of AR=5 ($\circ$) for reference.

The behavior of the flag in the flapping regime presents notable differences, with the existence of two distinct branches being no longer evident at most angles of attack. An abrupt increase in amplitude of motion and Strouhal number is present for the lower angles of attack ($\alpha \leqslant 6$), but no longer occurs at the flow speed at which the St value is maximum (figures 3.10 and 3.13). The Strouhal number slightly increases to then decrease linearly within the upper branch, with the flow velocity at which the Strouhal peaks being surprisingly equal for both aspect ratios ($\kappa^{1/2} \approx 2$). For higher α, however, all variables vary smoothly within the flapping regime, eliminating the distinction between the two branches. The absence of a marked upper branch results in lower amplitudes in the flapping motion for $\alpha > 8°$, with the difference in minimum deflection angle being particularly significant. The discrepancy initially occurs at the lower flow velocities exclusively, but extends to the full range for $\alpha > 14°$. The lowered amplitude of motion results in lower Strouhal numbers, making the underlying mechanism behind the flag's motion uncertain. Further investigation of this motion is necessary to clarify the flag's behavior and may reveal the existence of different branches that cannot be distinguished in the current data. The flag of AR=5 presented an additional discontinuity at a flow velocity of $\kappa^{1/2} \approx 1.5$ for angles $\alpha > 16$. Remarkably, this discontinuity is present at the same threshold and flow velocity in the AR=2 case.

The presence of a chaotic regime was also observed in the motion of the AR=2 flag, occurring at a larger range of flow velocities than the higher aspect ratio case. The data points corresponding to the chaotic region have been highlighted in black in figure 3.10. The velocity at which the flapping regime ceases to be present follows a linear trend with angle of attack, with, however, a more pronounced slope, that may be a result of variations in flow damping with aspect ratio. In this AR=2 case, the disappearance of the upper branch is associated to the decreasing deflection velocity, and therefore cannot be calculated in a similar manner. The full flapping motion, however, is practically non-existent at an angle of attack of $\alpha = 28°$.

An angle of attack of $\alpha = 30°$ was investigated in addition to those present in figures 3.10–3.13 and is presented in figure 3.14. Interestingly, a new resonant motion is clearly present. At the lower flow velocities, the power spectra of the motion show the existence of two peaks, which approximate each other as the large-amplitude motion is onset. This suggests the presence of a coupled-mode flutter mechanism. The nature of this motion is therefore distinct from that of the flapping motion analyzed throughout this chapter, and lies beyond the scope of this text. It

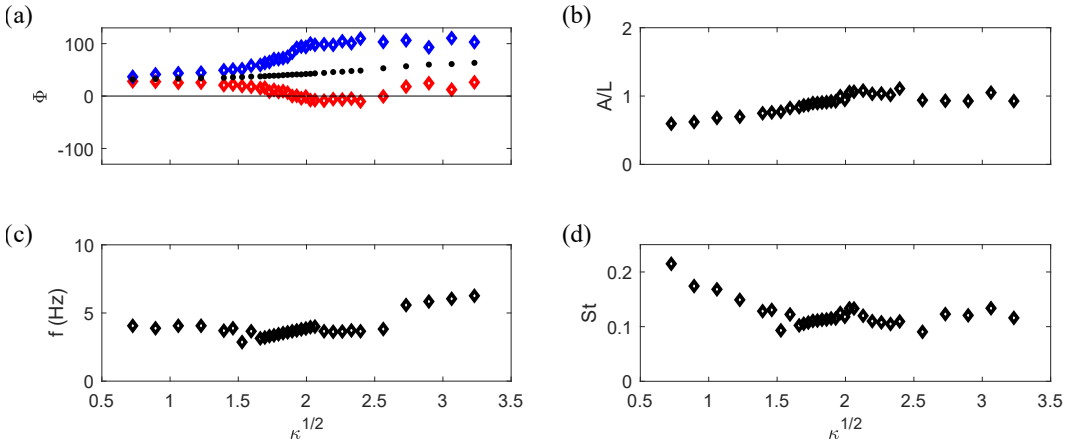

Figure 3.14: Behavior of an inverted flag of AR=2 at $\alpha = 30°$. Maximum (◇), minimum (◇) and mean (●) deflection angle, Φ, (b) maximum cross-section, A', (c) frequency of motion, f, and (d) Strouhal number, St

highlights, however, the variety of phenomena that may arise at angles of attack intermediate to the typically studied $\alpha = 0°,\ 90°$ and 180°, that may be of interest in future investigations.

3.2 Conclusions

This chapter has analyzed the effect of moderate angles of attack on the dynamics of an inverted flag. A flag of AR=5 was first investigated and showed results consistent with the existing literature at zero-angle-of attack, where the presence of a divergence instability was established experimentally for the first time. Three distinct dynamical regimes were identified at finite angles of attack: deformed, flapping and deflected. These correspond to small oscillations around a small deflection equilibrium, large-amplitude oscillations and small oscillations around a large deflection equilibrium, respectively. A new method that determines regions of resonance based on the power spectra of the motion was proposed as a means of identifying the initiation and cessation velocities of the flapping regime.

Unlike in the zero angle-of-attack case, the deformed state does not lose its stability through divergence. Instead, it was hypothesized that a galloping type instability gives rise to what has been denominated the lower branch of the flapping regime. At a constant non-dimensional flow velocity $\kappa^{1/2} = 2$ a second distinct branch within the flapping regime develops. This upper branch corresponds to the large-amplitude flapping motion that has been observed for the inverted flag at zero angle of attack and has been determined to be a vortex-induced vibration. As flow speed

is increased, the flag transitions to the deflected regime. The velocity at which this transition occurs decreases linearly with angle of attack, while the velocity at which the upper branch flapping is onset remains constant. This results in both velocities coinciding at an angle of attack of $\alpha = 26.8°$, beyond which the upper flapping branch ceases to exist. The entirety of the flapping motion further disappears at angles beyond $\alpha \approx 28°$.

A subsequent set of tests was performed on a flag of aspect ratio AR=2 and revealed contrasting dynamics. Although the three main dynamic regimes are still present, the distinction between lower and upper flapping branches is no longer evident. As a result, the angular amplitude of motion in the flapping regime is fairly decreased for angles of attack above $\alpha = 8°$.